

Received 8 July 2024, accepted 30 July 2024, date of publication 7 August 2024, date of current version 19 August 2024.

Digital Object Identifier 10.1109/ACCESS.2024.3439861

RESEARCH ARTICLE

Development of Residual Dense U-Net (RDU-Net)-Based Metal Artefacts Reduction Technique Using Spectral Photon Counting CT

OSAMA KHAN^{1,2}, BRIYA TARIQ¹, NADINE FRANCIS¹, NABIL MAALEJ¹,
ABDERAOUF BEHOUC³, AMER KASHIF², ASIM WARIS², (Member, IEEE),
AND AAMIR RAJA¹

¹Department of Physics, Khalifa University, Abu Dhabi, United Arab Emirates

²Department of Biomedical Engineering and Sciences, National University of Sciences & Technology, Islamabad 44000, Pakistan

³Department of Electrical Engineering and Computer Science, Khalifa University, Abu Dhabi, United Arab Emirates

Corresponding authors: Osama Khan (osama.khan@ku.ac.ae) and Aamir Raja (aamir.raja@ku.ac.ae)

This work was supported by the Research and Innovation Grant, Khalifa University of Science and Technology, Abu Dhabi, United Arab Emirates, under Grant 8474000563.

ABSTRACT Metal induced artefacts in computed tomography (CT) images are primarily caused by beam hardening, scatter effects, and photon starvation. These artefacts impede the characterization of fine anatomical structures and compromise the diagnostic value of the CT images. We aim to develop an innovative machine learning-based technique called residual dense U-Net (RDU-Net), specifically for spectral photon-counting CT (SPCCT), to mitigate metal artefacts across all energy bins. The proposed model was quantitatively evaluated, with and without the metal artefact reduction (MAR) algorithm, using line profiles, histogram analysis, signal-to-noise ratio (SNR), root mean squared error (RMSE), and structural similarity index measure (SSIM). The results show significant improvements with the average SNR increasing from 3.37 to 17.40 across the five energy bins after the application of the MAR algorithm. The average RMSE decreased from 0.016 to 0.001, and the average SSIM increased by 34.9%. The study also evaluated material density images of hydroxyapatite (HA) and iodine, with and without the MAR algorithm, using the receiver operating characteristic (ROC) paradigm. The results show improved accuracy in the material identification for HA (86% to 91%) and iodine (84% to 93%) after MAR. Overall, the evaluation of the model show promising results and the potential to significantly decrease the metal artefacts in all the parameters used in the energy analysis at $p < 0.0001$, while preserving the attenuation profile of SPCCT images.

INDEX TERMS Computed tomography (CT), metal artefacts reduction (MAR), spectral photon-counting CT (SPCCT).

I. INTRODUCTION

Computed Tomography (CT) is one of the most widely used diagnostic tool [1], [2], [3], [4]. It provides detailed high-resolution 3D views of the internal organs crucial for

The associate editor coordinating the review of this manuscript and approving it for publication was Sandra Costanzo¹.

diagnosing diseases such as cancer, cardiovascular disorders, and internal bleeding [5], [6], [7]. Additionally, CT images incorporate tissue density information, which is essential for radiation therapy treatment planning [8], [9]. However, one of the major challenges in CT imaging is the occurrence of metal artefacts due to the presence of high-density materials. These artefacts affect the assessment of tissues surrounding

metal structures, such as intracranial coils, clips, stents, dental or orthopedic implants, fixation devices, and other metal objects [10], [11], [12]. This limitation poses challenges in visualizing structures, hindering the detection of early-stage complications, such as inflammation, infection, tumors, and assessing the integration of metal implants into bone tissue. Metal artefacts distort CT scans due to beam hardening, scattering, photon starvation, and non-linear partial volume (NLPV) effects [13]. Beam hardening occurs mainly in polychromatic X-ray beams; low-energy photons are more readily absorbed by these materials leading to an increase in the average energy of the beam. This alters the path of the beam and leads to streaking, cupping artefact, and degradation of data integrity [14], [15]. Photon starvation occurs when metal objects absorb and restrict the number of photons within the beam, leading to insufficient photons reaching the detector. Such a reduced number of photon counts results in the increase of statistical noise due to deviation of the detected photon flux from the usual Poisson distribution [16]. NLPV effects arise from metal edges partially intersecting projection lines, causing inaccuracies in the calculation of attenuation coefficients and subsequent image reconstruction [17]. The combined effect of these artefacts may lead to imprecise outcomes. Accordingly, there is an increasing clinical demand to develop techniques to minimise metal artefacts. This demand has led to extensive research in this field, as shown in Fig. 1. While numerous studies focus on minimizing metal artefacts in CT images through specialized image reconstruction and processing algorithms [18], [19], [20], [21], [22], significant research is also focused on reducing these artefacts during the acquisition process, including but not limited to adjusting X-ray tube voltage and current, acquisition time, and voxel size [23], [24], [25], [26]. Despite employing these diverse techniques, conventional CT systems are inherently limited by the amount of information they can collect, primarily due to their reliance on single-energy spectrum X-ray sources and energy-integrating detectors. To address these limitations and facilitate a more thorough analysis, spectral photon-counting CT (SPCCT) with photon-counting and energy-discriminating detectors emerges as a promising solution. It possesses the capability to generate multiple images corresponding to different energy bins, providing more comprehensive spectral information for enhanced imaging and advanced analysis. It presents a significant transition in clinical imaging as it efficiently distinguishes between metals and surrounding tissues through the utilization of multi-energy data. Additionally, higher energies X-rays are less susceptible to metal artefacts, paving the way for the development of more efficient algorithms for the reduction of metal artefacts [27]. SPCCT employs photon-counting detectors (PCDs) with a single semiconductor diode layer, which applies high voltage directly without the need for photon-to-light conversion. This enables precise photon counting and improves the ability to differentiate between energy levels, which enhances contrast-to-noise ratios, spatial

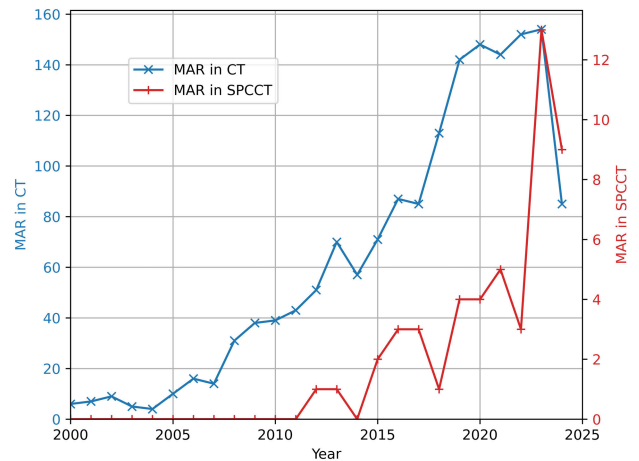


FIGURE 1. Illustration depicting the number of publications focused on metal artefact reduction (MAR) algorithms, comparing conventional CT techniques with the newer Spectral Photon Counting Computed Tomography (SPCCT) methods from January 2000 to June 2024. For conventional CT, the keywords used in Scopus were ('Metal artefact removal' OR 'MAR' OR 'Metal artefact removal' OR 'Metal artefact reduction' OR 'Metal artefact reduction') AND ('Computed Tomography' OR 'CT'). For SPCCT, these keywords were combined with ('Spectral Computed Tomography' OR 'Spectral CT' OR 'PCCT' OR 'Photon Counting CT' OR 'Photon Counting Computed Tomography' OR 'SPCCT' OR 'Spectral Photon Counting CT' OR 'Spectral Photon Counting Computed Tomography') AND NOT ('Dual Energy CT' OR 'DECT' OR 'Dual Energy Computed Tomography').

resolution, and minimizes radiation exposure and electronic noise [28], [29]. SPCCT also opens a gateway for new medical applications, such as precise material identification and quantification, commonly known as material decomposition (MD) [30], [31]. MD involves calculating material-specific basis vectors using multi-energy data from SPCCT and decomposing materials into accurate density images. This can further aid in early diagnosis, improve anatomical visualization, and facilitate the detection of diverse conditions, such as bone diseases, soft tissue abnormalities, cancer imaging with nanoparticles, crystal-induced arthritis, and imaging in the presence of metal implants [32], [33], [34]. Besides technological advancements, metal artefact reduction (MAR) can be accomplished through the utilization of complex and sophisticated computational techniques, commonly referred to as MAR algorithms. MAR algorithms detect and segment the corrupted data caused by metal implants, and further modify and replace the corrupted data with estimates of the corrected values. MAR algorithms are applied either in the sinogram/projection domain (consists of the projection data) or in the image domain (consists of reconstructed images) or in a combination of both called dual domain [35]. Sinogram domain methods treat metal-affected regions in sinograms as if they are missing and replace them using interpolation or forward projection. However, this approach would introduce streak artefacts tangent to the metal objects, as it is challenging to avoid discontinuities in the sinogram [36]. For image-based metal segmentation methods, the metal region is segmented in the reconstruction

images and is forward-projected to localize the projection data that the metal has contaminated. Moreover, many of the available MAR algorithms employ the image-based metal segmentation method due to restricted access to the raw data [37], [38], [39]. In recent years, deep learning-based MAR methods have emerged as promising tools in medical imaging, demonstrating reliable results [40]. For instance, Zhang et al. presented a convolutional neural network (CNN) MAR model as an open artefact reduction framework for CT, capable of distinguishing tissue structures from the artefacts and fusing the useful information to generate CNN images. By utilizing the designed tissue processing technique, artefacts are suppressed to generate a high-quality prior image. Both clinical and numerical simulations have shown that CNN-MAR can reduce metal artefacts and restore fine structures near the metals to a large extent [41]. Lin et al. also developed a deep learning architecture named an end-to-end trainable Dual Domain Network (DuDoNet), which simultaneously enhances CT images and restores the sinogram consistency to solve the problem of metal artefacts. The model consists of a radon inversion layer, a sinogram enhancement network (SE-Net), and an image enhancement network (IE-Net). Results show that DuDoNET has outperformed many MAR techniques, such as normalized MAR (NMAR) and CNN-MAR, through the superior peak signal-to-noise ratio (SNR) and structural similarity index measure (SSIM) values with lesser computational time [42]. Furthermore, Hegazy et al. introduced the U-NET model for MAR in dental CT and compared four different configurations of CT i.e., Unet-64, Unet-32, Unet-16, and Unet-8. These experiments have shown that the computation speeds in Unet-32 and Unet-16 increased about 3.6 and 7.3 times compared to Unet-64, respectively. As a result, Unet-16 could segment the metal regions with accuracy very close to the original U-net and even with 7.3 times faster computation speed [43]. Zhuoxing et al. introduced a deep learning-based method to address metal artefacts in dual-energy CT; the approach synthesizes triple-energy spectral CT datasets and employs CNN to generate virtual monochromatic images (VMIs), effectively reducing artefact-induced streaks. Results show significant artefact reduction through simulations on an abdominal phantom, with root mean square error (RMSE) reaching below 30 Hounsfield units (HU). This work emphasizes the benefits of dual-energy CT in material discrimination and show how deep learning frameworks can improve image quality without raising patient dose levels [44].

Busi et al. presented a significant contribution focusing on spectral deep learning to mitigate metal artefacts in spectral X-ray computed tomography (SCT), utilizing photon counting detectors. Their study proposed a 3D U-Net architecture for metal artefact reduction in spectral X-ray CT to handle the large 3D matrices of spectral images. The method faces limitations due to high computational demands, hardware constraints leading to loss of detail, and biased training from highly attenuating materials like

metals. To address these, the study proposes high attenuation thresholding and normalization steps. However, challenges persist in representing geometric shapes and preserving effective linear attenuation coefficients [45]. This highlights the necessity for more effective models to manage spectral data. As shown in Fig. 1, there is a noticeable research gap in MAR algorithms for SPCCT, suggesting numerous avenues for additional exploration in this field.

We aim to introduce a novel MAR algorithm based on a residual dense U-Net (RDU-Net) deep learning architecture. The proposed algorithm simultaneously corrects artefacts across all energy bins of SPCCT. To achieve this, we used a commercially available Mars SPCCT scanner installed in our laboratory to acquire multi-energy CT images. Results were evaluated quantitatively using line profiles for spatial assessments, histograms for CT values analysis, along with SNR, root mean squared error (RMSE), SSIM, and receiver operating characteristic (ROC).

II. MATERIALS AND METHODS

A. PHANTOM CONFIGURATIONS AND DISTRIBUTION OF DATASETS

We used a 100 mm-diameter QRM Spectral CT phantom (QRM, GbH, Moehrendrof, Germany) consisting of 20 mm-diameter holes to hold eight multiple solid inserts. Ten scans of the QRM phantom were taken in order to generate ten datasets: Six datasets were used for training the MAR algorithm, two datasets for generating simulated images, and the remaining two datasets were used for the validation of MAR algorithm as shown in Fig. 2. The overall distribution and utilization of the datasets are summarized in Table 1. Training datasets include two types of datasets: one dataset comprises variations in the placements of aluminium (99% Al; 20 mm-diameter) and steel (surgical stainless steel; 20 mm-diameter) Fig. 2 (a-d)), while the other dataset consists of varying concentrations of hydroxyapatite (HA) (201.4 and 406.9 mg/cm³) and iodine (9.66 and 14.56 mg/cm³), along with adipose, and CT water in the presence of aluminium and steel (shown in Fig. 2 (e,f)). The training datasets comprised a scan length of 50 mm along the scanner data acquisition axis: 20 mm containing metal inserts, followed by 10 mm eliminated length (not used for analysis) to prevent the detection of residual artefacts, and 20 mm used as an empty phantom for generating simulated images, as illustrated in Fig. 3. Datasets for Simulation (Fig. 2 (g,h)) were used to extract metal-specific attenuation profiles of aluminium and steel. After the training of the MAR model, we assessed its performance using two validation datasets: the first dataset consisted of aluminium and steel, while the second dataset included varying concentrations of HA and iodine, along with muscle, and CT water in the presence of an aluminium insert, as shown in Fig. 2 (i,j).

B. SCANNER CONFIGURATION

All datasets were collected using the small bore MARS SPCCT scanner (MARS Microlab 5 × 120). MARS

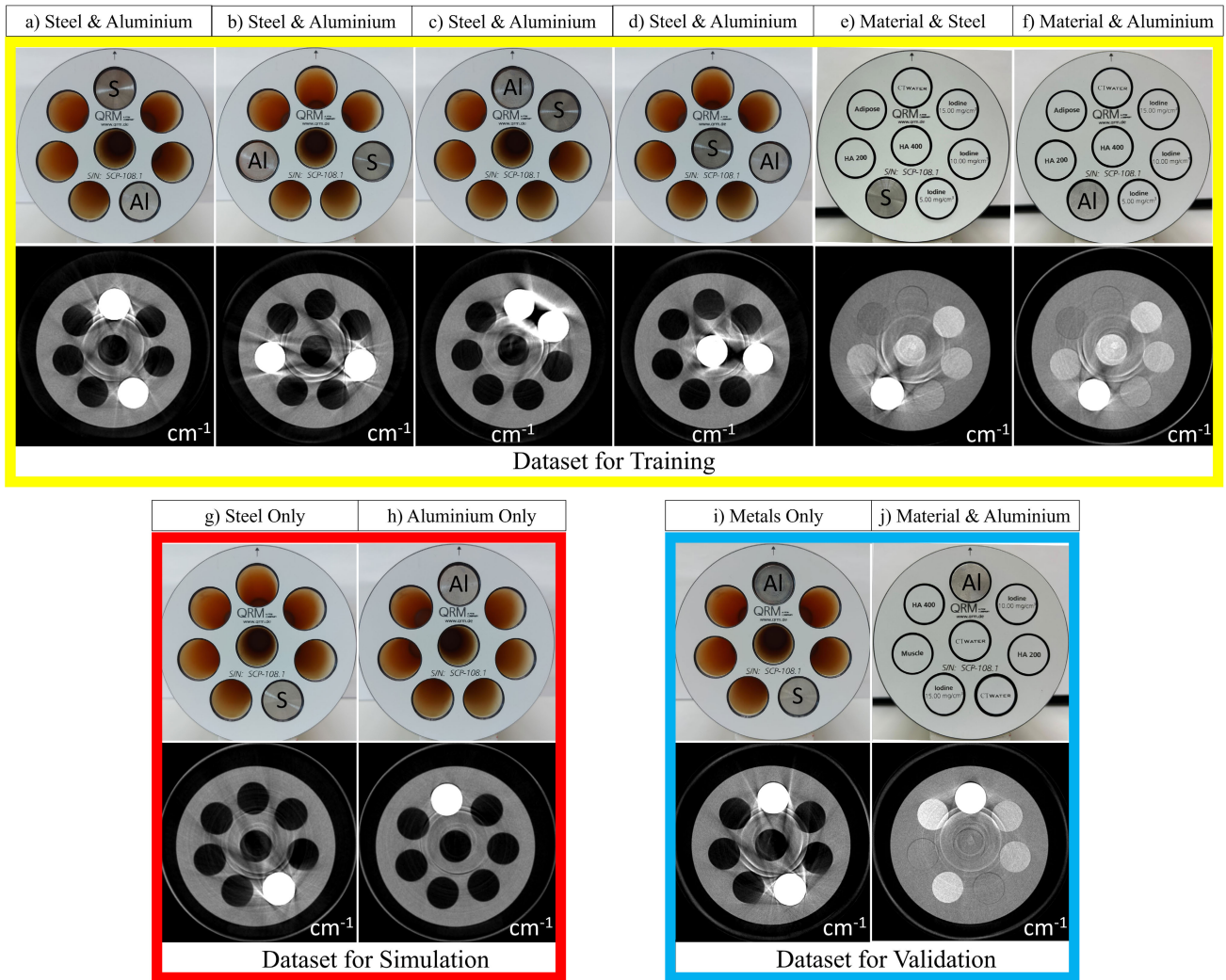


FIGURE 2. Illustration of different phantom configurations and their corresponding CT images across first energy bin (7-40 keV) acquired at 118 kVp with 80 μ A tube current. The training datasets (yellow block) consist of varying placements of steel and aluminium (a-d), while (e, f) contained two concentrations of hydroxyapatite HA (201.4 and 406.9 mg/cm³) and iodine (9.66, and 14.56 mg/cm³), along with adipose, CT, and water in the presence of metal inserts; steel (e) and aluminium insert (f). The red block shows datasets used for simulation (g,h), consisting of only steel or aluminium inserts for extracting material-specific attenuation profiles. Validation datasets are shown in the blue block; a dataset that includes both metal inserts (i), and (j) a dataset that includes material inserts in the presence of aluminium insert. All energy images are scaled in linear attenuation coefficients (cm⁻¹) in the range of 0 to 0.3 cm⁻¹. The label 'S' and 'Al' refers to steel and aluminium respectively.

SPCCT integrates conventional CT principles with spectral imaging utilizing Medipix3RX PCDs. Medipix3RX PCDs measure individual detected photons exceeding the user-defined energy thresholds and process these signals through electronic comparators and counters to calculate photon counts [46]. The Medipix3RX chip gives MARS SPCCT the ability to acquire multi-energy data for up to 8 energy bins. The scanner is comprised of a microfocus poly-energetic X-ray source (Source Ray SB-120-350, SourceRay Inc, Bohemia, NY) with an additional 1.8 mm Al equivalent intrinsic filtration, and 0.125 mm external brass filtration. All scans were performed using 118 kVp tube voltage, 981 circular projections with an exposure time of 160 ms per frame. The tube current was set at 80 μ A to maintain a photon count rate less than 11 counts/ms to avoid detector saturation

and pulse pileup [47]. All scans were performed in the charge-summing mode using the default energy thresholds of 40, 50, 60, and 79 keV. The data were reconstructed using the proprietary MARS iterative reconstruction technique in the narrow energy bins, 7-40, 40-50, 50-60, 60-79, and 79-118 keV. The resulting images have an isotropic voxel size of 0.1 mm and an image matrix of 1300 \times 1300.

C. CREATION OF ARTEFACT-FREE SIMULATED DATA

Any supervised deep learning-based MAR technique requires artefact-free images for model training. For this task, simulated images were generated using an automated strategy developed in Python (Python 3.10.12). Datasets for simulation depicted in Fig. 2 (g,h) were employed to calculate the mean attenuation (1) and standard deviation (2) values

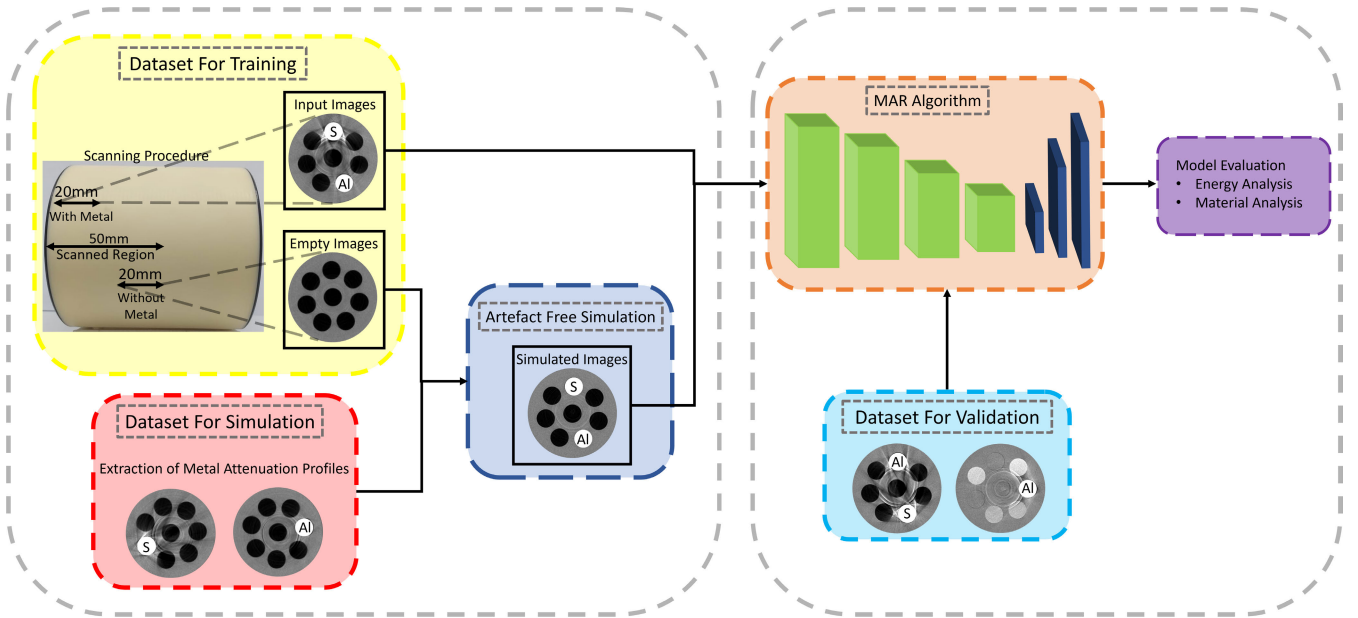


FIGURE 3. Demonstration of step-by-step methodological pipeline. Different sections show the acquisition, processing, and utilization of datasets for the training, simulation, and validation of the MAR algorithm. The label ‘S’ and ‘Al’ refers to steel and aluminium respectively. The left block indicates the training and simulation section. The total scan length was 50 mm along the scanner data acquisition axis: the first 20 mm contained metal inserts was used as input training datasets and the last 20 mm was used as an empty phantom for generating simulated images. The dataset for simulation provides the attenuation profile for steel and aluminium to simulate the artefact-free images using empty images. The right block depicts the process of how the datasets for validation were used for testing the algorithm.

TABLE 1. Summary of Datasets for Training, Simulation, Validation (Fig. 2) and Evaluation Strategy for validation of Metal Artefact Reduction (MAR) Algorithm.

Phantom Description		Datasets for Training			Datasets for Simulation		Datasets for Validation	
		Phantom with steel-aluminium placement variation	Phantom with steel and materials	Phantom with aluminium and materials	Phantom with aluminium insert only	Phantom with steel insert only	Phantom with steel and aluminium inserts only	Phantom with aluminium and materials
Demonstration		Fig 2 (a-d)	Fig 2 (e-f)		Fig 2 (g-h)		Fig 2 (i - j)	
Training Dataset		Provides 20mm Input Scan			—	—	—	—
Artefact Free Simulation		Provides 20mm Empty Scan			Extraction of material specific linear attenuation profiles		—	—
Evaluation Strategy	Energy Analysis	—	—	—	—	—	Line profile, histogram, SNR, RMSE & SSIM	—
	Material Analysis	—	—	—	—	—	—	Material decomposition, sensitivity, specificity, accuracy, NPV, PPV, RMSE

across five energy bins for aluminium and steel. The scan of each metal was done separately to ensure the extraction of metal-specific profiles without any external factors influencing the results. The values were then superimposed throughout the images of the empty phantoms, acquired from the training dataset (shown in Fig. 2 (a-f)), to obtain artefact-free ground truths for the model training.

$$\mu = \frac{1}{N_{mt}} \sum_{i=1}^{N_{mt}} (MT_{pix_i}) \quad (1)$$

$$\sigma = \sqrt{\frac{1}{N_{mt} - 1} \sum_{i=1}^{N_{mt}} (MT_{pix_i} - \mu)^2} \quad (2)$$

where:

- μ is the mean attenuation value of the metal insert ROI.
- σ is the standard deviation of the the metal insert ROI.
- N_{mt} represents the number of pixel values.
- MT_{pix_i} represents individual pixel values.

D. DEEP LEARNING MAR ALGORITHM

A SPCCT image array denoted by $I \in \mathbb{R}^{E \times L \times W}$, where \mathbb{R} is a set of real numbers, E is the number of energy bins, L is the length of the image, and W is the width of the image. A deep learning model is trained to generate an artefact free image array $M \in \mathbb{R}^{E \times L \times W}$. This process of MAR is expressed as $M = f(I; \theta)$, where ' θ ' contains the learnable parameter of the model. The proposed MAR algorithm employs a

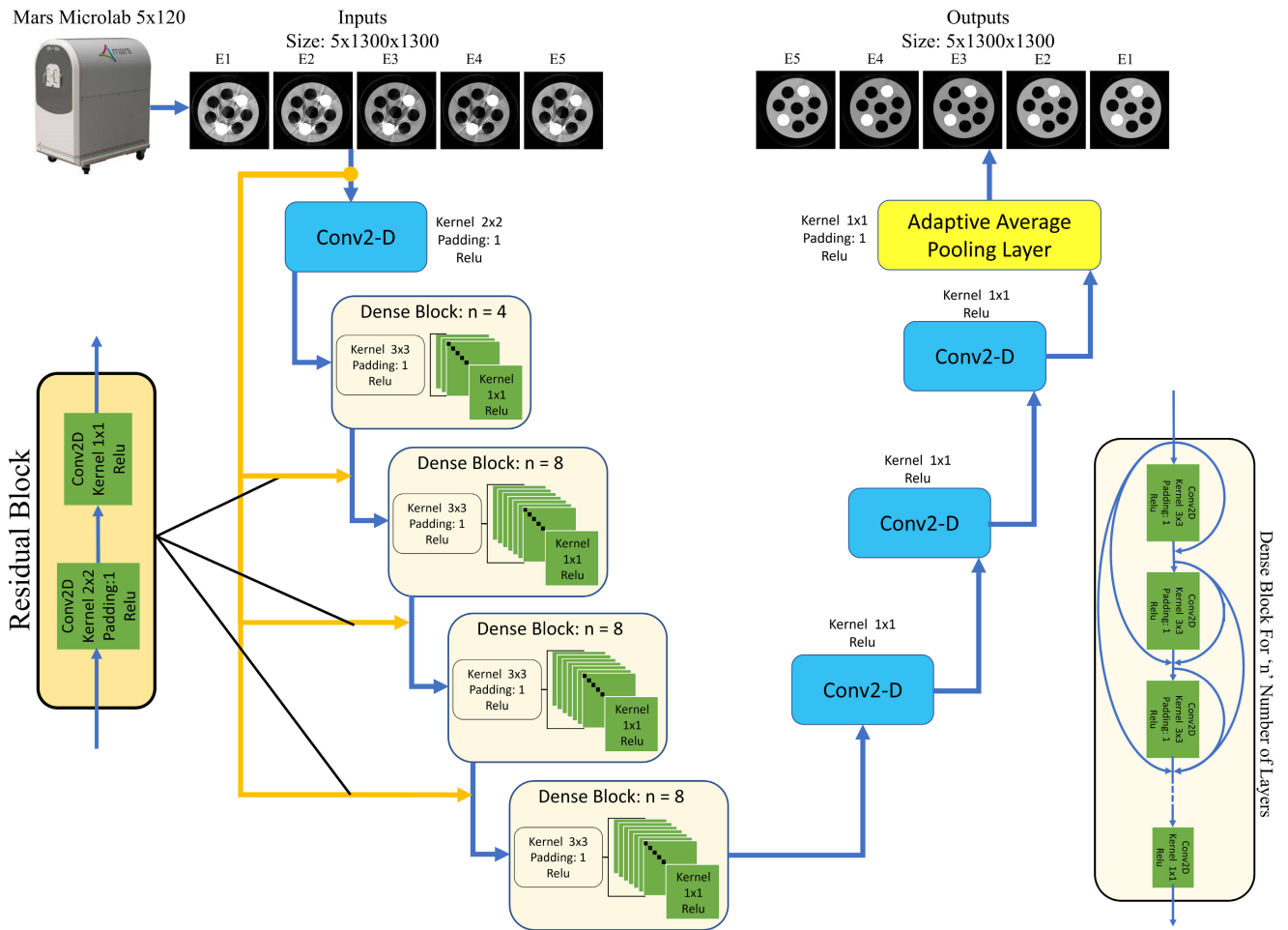


FIGURE 4. Overall architecture and functioning of the RDU-Net model For MAR. The RDU-Net model is an encoder-decoder-based architecture. The encoder block consists of four dense blocks and three residual connections. The decoder consists of three convolution layers followed by an adaptive average pooling layer. The figure shows corrected metal artefacts of spectral photon-counting multi-energy CT images as outputs by applying the proposed MAR algorithm. E1 (7-40 keV), E2 (40-50 keV), E3 (50-60 keV), E4 (60-79 keV), and E5 (79-118 keV) represent the five energy bins. Conv2D refers to two-dimensional convolution layers, while ‘n’ is the number of connected layers in the dense block.

deep learning approach based on RDU-Net, performing image-to-image transformation. The model combines ResNet (Residual Network) [48], DenseNet [49], and U-Net [50] architectures to create the RDU-Net architecture which was implemented using the PyTorch library, as shown in Fig. 4.

1) RESNET

ResNet model was developed to tackle the problem of vanishing gradients in deep neural networks. The vanishing gradient problem arises when gradients decrease exponentially during back-propagation in deep neural networks, impeding the training process and leading to degradation in performance. ResNet addresses this issue by incorporating residual connections, which enable the model to learn residual functions. This innovation allows the training of deeper networks without a deterioration in performance. Through the integration of residual connections, ResNet models achieve state-of-the-art

performance in various image recognition tasks whilst being more straightforward to optimize and train when compared to traditional deep networks.

2) DENSENET

DenseNet model, or Densely Connected Convolutional Networks, introduces dense connectivity patterns between layers, where each layer receives feature maps from all preceding layers. This dense interconnection facilitates feature reuse and gradient flow, promoting deeper networks with fewer parameters. This leads to improved feature propagation, ultimately enhancing model performance and training efficiency.

3) U-NET

U-Net is a convolutional neural network architecture designed for biomedical image segmentation tasks. It features a U-shaped architecture with an encoder-decoder structure,

where the encoder extracts high-level features and the decoder performs pixel-wise classification. Additionally, U-Net incorporates skip connections between corresponding encoder and decoder layers to preserve spatial information and facilitate precise segmentation.

4) PROPOSED METHOD

The RDU-Net architecture features an entry channel of $5 \times 1300 \times 1300$ and is structured around a U-net type encoder-decoder backbone. The encoder module consists of 4 dense blocks and 3 residual layers, as shown in Fig. 4. The dense block is denoted by $D = X_0 \oplus f_1(X_0; \theta_1) \dots \oplus f_n(X_{n-1}; \theta_n)$, where X represents the feature map, \oplus represents the concatenation operation, f represents the convolution function, and n represents the number of layers in the dense block. The dense block connects each layer to every other layer in a feed-forward fashion by concatenating features after every layer. This dense connectivity facilitates feature reuse, encourages feature propagation, and enhances gradient flow throughout the network, which result in more efficient feature extraction. The first dense layer consists of 4 connected layers while each of the remaining three consists of 8 connected layers. All convolution layers in the dense block had a kernel size of 3×3 , padding of 1, and ReLU activation function, except the last layer in each dense block, which had a kernel size of 1×1 , no padding, and ReLU activation function. The residual layers includes two 2D convolution layers: the first one with a kernel size of 2×2 , padding of 1, and ReLU activation function; and the second one with a kernel size of 1×1 , no padding, and ReLU activation function. The three residual layers establish connections between the input and the dense layers, thereby mitigating the risk of gradient vanishing and preserving features from the input. Subsequently, the decoder comprises three 2D convolution layers, with kernel size 1×1 , no padding and ReLU activation, to reconstruct the encoded image back to its original input format. An adaptive average pooling layer is applied following the encoder-decoder sequence adjusting the output dimensions to match those of the input. For model training, we employed L1 Loss Function along with Adam optimizer, utilizing a learning rate of 0.001. Various loss functions, including mean squared error (MSE) and binary cross entropy (BCE) loss, were tested, but L1 loss [51] gave more distinct boundaries and sharper images with reduced noise. MSE loss also yielded comparable results; however, due to its tendency to dampen smaller errors, it did not effectively mitigate lighter streaks and noise in our scenario, where the majority of attenuation values are small. Adam optimizer was chosen for our problem. It was selected because of its adaptive learning rate, efficiency with sparse gradients, and regularization benefits. These qualities are crucial for handling complex spectral data. Other optimizers, such as SGD and RMSprop, are less suitable. They handle sparse gradients less efficiently and have slower convergence rates in complex models like the RDU-Net. The utilization

of adam optimizer contributed to faster convergence of gradients, leading to a quicker and more accurate reduction in loss. This resulted in a decreased number of epochs required for convergence. We settled on a learning rate of 0.001 after experimenting with different values. Higher learning rates were ineffective due to our small pixel values. Lower rates, on the other hand, resulted in excessively slow training because of the large size of the image slice ($5 \times 1300 \times 1300$). Thus, we opted for the lowest effective learning rate that consistently delivered satisfactory results. The model was trained on an HPC node equipped with two Nvidia V100 GPUs, each with 32 GB of memory. The overall steps employed in this study to train and validate the RDU-Net model are depicted in Fig. 3 and Fig. 4.

E. EVALUATION STRATEGY

The evaluation of the RDU-Net-driven MAR algorithm involves two distinct phases: validation using a dataset containing only metal inserts, and validation using a dataset encompassing both materials and metal inserts. The initial validation of the first dataset includes the analysis of images across five discrete energy bins, referred to as ‘‘Energy Analysis’’. The second evaluation of the second dataset involves the utilization of density images, identified as ‘‘Material Analysis.’’

1) ENERGY ANALYSIS

Energy analysis of the obtained results was performed using four techniques. The spectral response of the first validation dataset (Fig. 2 (i)) was analyzed using line profiles (with a length of 30 mm) through the center of the inserts. These lines were consistently positioned across all five energy bin images for input, simulated, and output images, see Fig. 6 (a,e). Cumulative histograms for the six regions of interests (ROIs), as indicated in Fig. 7 (a), across all five energy bins were plotted to evaluate the distribution of the linear attenuation values in input, simulated, and output images.

For the statistical assessment, SNR and RMSE were calculated within the same six ROIs using (3) and (4) respectively. SNR represents the ratio between the mean attenuation and the standard deviation values inside the ROI. A higher SNR indicates that the signal is more prominent relative to the noise, which generally corresponds to a clearer and more accurate representation of the imaged structures.

$$SNR = \frac{\mu}{\sigma} \quad (3)$$

The RMSE measures the square root of the average of the square error between the corresponding values of the input and simulated images and between the output and the simulated images. It is a standard measure for the differences between values of inputs and outputs with respect to the simulated images. A lower RMSE value is indicative of more

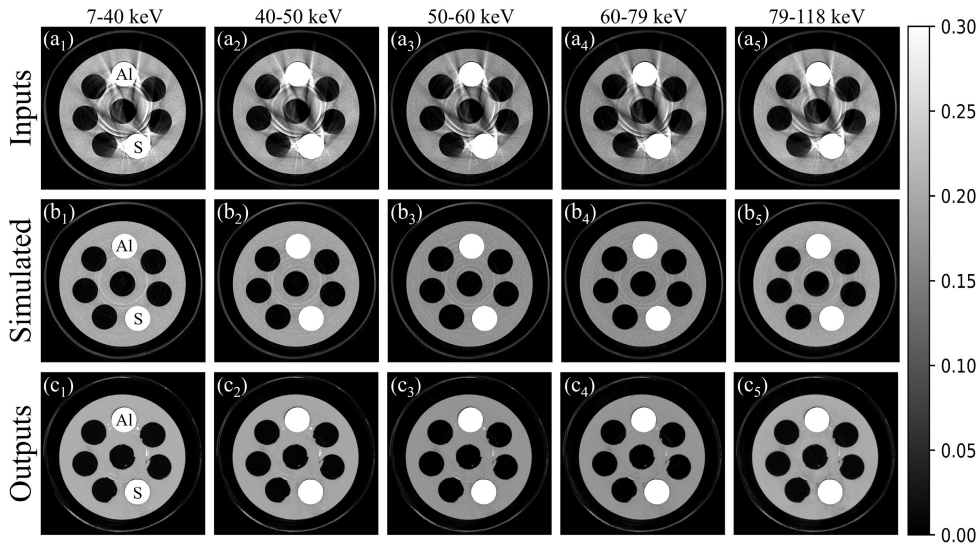


FIGURE 5. Illustration of the validation dataset shown in Fig. 2(f). (a) Input images acquired at 118 kVp and 80 μ A across five energy bins. (b) simulated images created using mathematical simulation to generate artefact-free reference images. (c) output images are the corrected input images (from (a)) using the proposed RDU-Net model. The grayscale bar represents the linear attenuation coefficient range from 0 to 0.3 cm^{-1} concatenation. The label 'S' and 'Al' refers to steel and aluminium respectively.

optimal results.

$$RMSE = \sqrt{\frac{1}{n} \sum_{i=1}^n (x_i - y_i)^2} \quad (4)$$

where:

- x_i and y_i are the corresponding pixel values of the original and reconstructed images.
- n is the total number of pixels in the image.

The structural similarity index (SSIM) (5) was used to quantitatively evaluate the similarity across the entire scanned phantom, as shown in Fig. 8 (d). The SSIM measures the structural similarity, luminance, and contrast between two images to provide a value between -1 and 1 ; where 1 indicates perfect similarity.

$$SSIM(x, y) = \frac{(2\mu_x\mu_y + C_1)(2\sigma_{xy} + C_2)}{(\mu_x^2 + \mu_y^2 + C_1)(\sigma_x^2 + \sigma_y^2 + C_2)} \quad (5)$$

where:

- x and y are the two compared images.
- μ_x and μ_y are the mean attenuation values of the ROIs in images x and y .
- σ_x^2 and σ_y^2 are the variances of the attenuation values of the ROIs in images x and y .
- σ_{xy} is the covariance of x and y .
- C_1 and C_2 are constants to stabilize the division with a weak denominator.

A standard independent-2 sample t-test, that assumes equal population variances, was performed on the following three metrics of evaluation in order to calculate the p-values and assess if the observed change was significant. A comparative study was conducted to ascertain the performance of the

proposed model against two state-of-the-art machine learning algorithms, U-Net [50] and VGG-16 [52]. Both U-Net and VGG-16 have been extensively used for image recognition and segmentation tasks in medical imaging [53], [54], [55]. All three models were trained for 200 epochs on the same training dataset. The performance was quantitatively assessed using Peak Signal-to-Noise Ratio (PSNR), SSIM and RMSE. These metrics were then used to evaluate and compare the results of each model.

2) MATERIAL ANALYSIS

The material analysis was conducted using the validation dataset that contain materials and metal inserts (as shown in Fig. 2 (j)). The evaluation was performed using the effect of MAR algorithm on material identification and quantification obtained through MD on CT images. All energy images were converted to material density images using vendor-provided MARS-FASTMD v1.4 software. The software uses the basis vectors and the linear least squares estimation to predict the material combinations and concentrations from the attenuation profiles [30]. Additional details on Mars MD can be found in [56]. The MD algorithm was utilized to decompose input and output images, both with and without MAR algorithm, into HA and iodine density images. The QRM phantom contained two concentrations of HA (201.4 and 406.9 mg/cm^3) and iodine (9.66 and 14.56 mg/cm^3), along with water and muscle. Material decomposition were quantitatively assessed using Python 3.10.12. The sensitivity was determined by comparing voxel counts in a ROI for the target material in density images against ground truth energy images. The specificity was evaluated for the entire density image ROI against the target

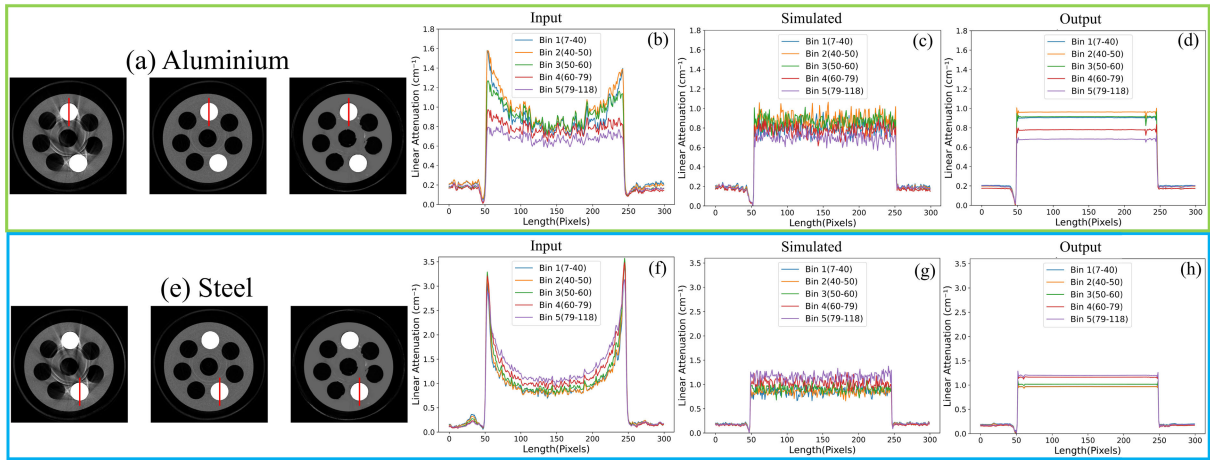


FIGURE 6. Depiction of line profiles passing through the center of metal inserts. The line profiles of 30 mm in length, (illustrated in red color in (a) and (e)) show the assessment of linear attenuation profiles and cupping artefacts in the input, simulated, and output images across the five energy bins of the validation datasets (shown in Fig. 5).

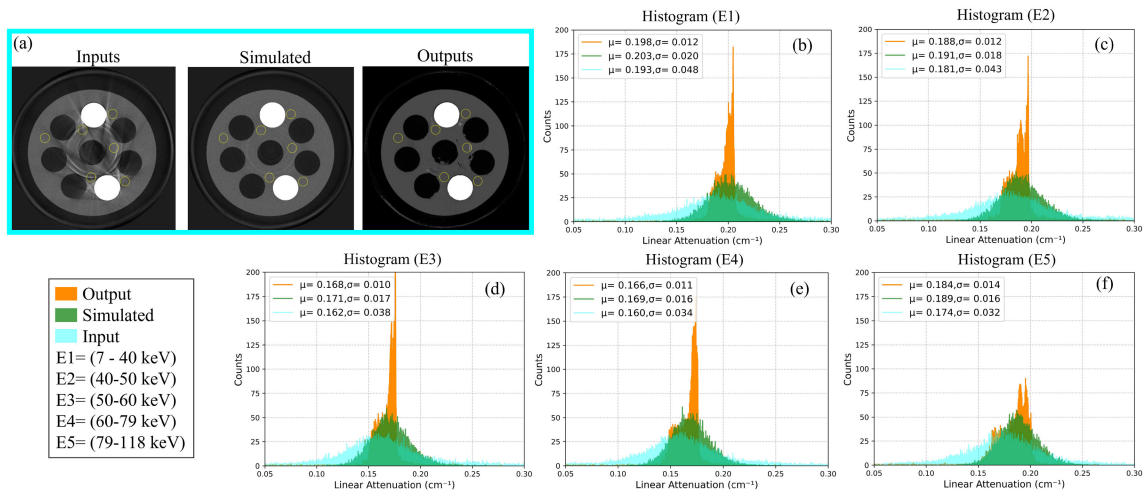


FIGURE 7. The Histogram analysis of the validation dataset shown in Fig. 5. (a) Six Region of Interests, indicated by the yellow circles, were used to plot the cumulative histograms of pixel values of the input, simulated, and output images across five energy bins (b-f).

TABLE 2. Statistical results of evaluation metrics: SNR (signal-to-noise ratio), RMSE (root mean square error), and SSIM (structural similarity index) with respect to simulated images.

Energy Bins	Signal-to-Noise Ratio (SNR)		Structural Similarity Index Measure (SSIM)		Root Mean Square Error (RMSE)	
	Input	Output	Input	Output	Input	Output
E1 (7-40keV)	3.12 ± 0.19	19.08 ± 2.08	0.539 ± 0.007	0.740 ± 0.004	0.0114 ± 0.004	0.0039 ± 0.002
E2 (40-50keV)	3.18 ± 0.22	18.01 ± 1.87	0.538 ± 0.007	0.742 ± 0.004	0.0149 ± 0.004	0.0016 ± 0.002
E3 (50-60keV)	3.19 ± 0.23	18.68 ± 1.85	0.544 ± 0.007	0.752 ± 0.004	0.0181 ± 0.004	0.0011 ± 0.001
E4 (60-79keV)	3.44 ± 0.22	18.30 ± 1.62	0.557 ± 0.007	0.751 ± 0.003	0.0182 ± 0.003	0.0013 ± 0.001
E5 (79-118keV)	4.32 ± 0.19	15.90 ± 1.03	0.611 ± 0.006	0.769 ± 0.004	0.0087 ± 0.001	0.0013 ± 0.002
Average	3.45	17.99	0.558	0.751	0.0143	0.0018

material ROI. The comprehensive quantitative assessment encompassed additional metrics, including accuracy, positive predicted value (PPV), and negative predicted value (NPV).

III. RESULTS

A. ENERGY ANALYSIS

In this section, we present the results of the energy analysis using our proposed machine learning model. Fig. 5 shows the

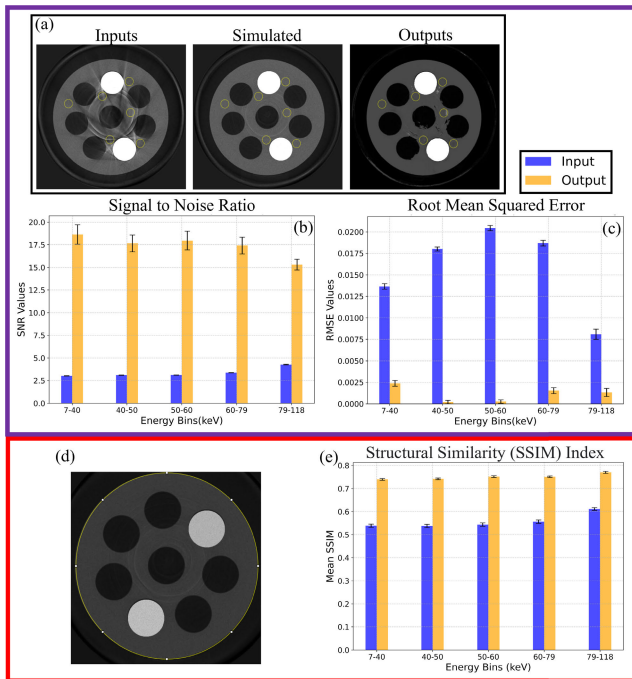


FIGURE 8. The Evaluation metrics for the MAR algorithm. (a) The Region of Interests (ROIs) used for SNR and RMSE calculations. (b) Graph for input and output SNR and (c) RMSE values of input to output calculated with respect to the simulated images. (d) The ROI for SSIM calculation, and (e) SSIM of the input and output images with respect to simulated images.

validation dataset we used for this analysis. The input images included various prominent artefacts including streaking, increased noise, as well as deep ring artefacts that were enhanced in the presence of metals. The qualitative evaluation of the output images, after the application of MAR, shows a considerable decrease in these artefacts. Nevertheless, a subtle spatial distortion was observed in the output images, particularly in regions impacted by ring artefacts and in close proximity to metals. However, the extent of this distortion progressively diminishes from Fig. 5 (c₁) to (c₅) as the energy level increases.

Fig. 6 illustrates the line profiles of the linear attenuation coefficient across both aluminum and steel metal inserts. The line profiles show gross overestimation of linear attenuation coefficients at the edges of the metal inserts, which can be observed as two steep peaks seen in the line profiles of Fig. 6 (b) for aluminium and Fig. 6 (f) for steel. Furthermore, it is noticeable that this overestimation is particularly pronounced in steel, which consistently displays elevated levels of noise even at higher energies. In contrast, for aluminum, the height of the peaks diminishes, indicating a reduction in artefacts and noise compared to steel. Fig. 6 (d,h) show how the utilization of the RDU-Net model eliminates metal artefact, reduces the noise, and produces sharper edges.

Fig. 7 demonstrates the spread of pixel values along the phantom body. The histogram analysis reveals consistently narrower spreads in the output images, indicating lower noise effects compared to the input images.

Fig. 8 shows the graphical representation of the evaluation metrics, while Table 2 provides the quantified values. Fig. 8 (a) shows the ROIs that were selected in order to calculate SNR and RMSE results. SNR results, calculated for the input and output images across the five energy bins, are shown in Fig. 8 (b). Furthermore, Fig. 8 (c) and (e) show the comparison of RMSE and SSIM values, respectively, between input and simulated images, as well as between output and simulated images. A student t-test was performed on these results and demonstrated significant changes with p-values < 0.0001.

Table 3 demonstrates the results of the comparative study, revealing the superior performance of the proposed RDU-Net model. The RDU-Net model surpasses the other two state-of-the-art models (U-Net and VGG-16) in all metrics across all energy bins. This highlights its increased ability to efficiently handle spectral data, significantly reducing noise and artefacts simultaneously across all energy bins.

B. MATERIAL ANALYSIS

In this section, we present the results of the material analysis using our proposed machine learning model. Fig. 9 (b) and (c) show the phantom material density images of both HA and iodine without MAR. On the other hand, Fig. 9 (f) and (g) show the phantom material density images of HA and iodine after the application of the proposed MAR algorithm. Following the implementation of MAR algorithm, an improvement in the accuracy of the MD was observed. Artefacts misclassified as HA and iodine were properly identified and corrected after the application of MAR. In Fig. 9 (d) and (h), the voxel-wise distribution of HA and iodine is depicted based on known concentrations, with and without MAR algorithm, utilizing the box and whiskers plot. Smaller size of these plots for both materials highlight reduction in the material density distributions when MAR algorithm is applied. Performance parameters including, sensitivity, specificity, accuracy, NPV, and PPV for the material density images of HA and iodine, with and without MAR are shown in Table 4.

IV. DISCUSSION

The proposed RDU-Net MAR algorithm in this study is specifically designed to correct multi-energy SPCCT images. It capitalizes on the inherent artefact reduction capabilities of SPCCT at the data acquisition level and during the reconstruction algorithms, especially in higher energy bins. Our methodology leverages these inherent benefits of the image domain, resulting in increased algorithm efficiency and superior outcomes. Overall, the RDU-Net exhibits good performance across all evaluated metrics, as demonstrated in the results section. It effectively mitigates artefacts induced by metallic objects while accurately preserving multi-energy attenuation characteristics. This capability ensures the retention of spectral data integrity and the post-artefact correction. The algorithm was evaluated in the energy and material domain to quantitatively assess its effectiveness.

TABLE 3. Qualitative Assessment of RDU-Net, Unet, and VGG16 across the five energy bins. The assessment was conducted on the validation dataset in Fig. 5. The best results for each assessment are highlighted.

Energy Bins (keV)	Peak Signal-to-Noise Ratio (PSNR)			Structural Similarity Index Measure (SSIM)			Root Mean Square Error (RMSE)		
	RDU-Net	Unet	VGG16	RDU-Net	Unet	VGG16	RDU-Net	Unet	VGG16
7-40	23.69 ± 0.17	15.66 ± 0.77	15.14 ± 0.74	0.738 ± 0.002	0.603 ± 0.005	0.574 ± 0.001	0.065 ± 0.001	0.165 ± 0.013	0.175 ± 0.014
40-50	23.99 ± 0.13	15.62 ± 0.78	14.72 ± 0.72	0.738 ± 0.002	0.572 ± 0.003	0.559 ± 0.001	0.063 ± 0.001	0.166 ± 0.014	0.184 ± 0.014
50-60	23.07 ± 0.25	14.85 ± 0.66	14.22 ± 0.63	0.751 ± 0.002	0.494 ± 0.003	0.534 ± 0.001	0.070 ± 0.002	0.181 ± 0.013	0.195 ± 0.013
60-79	17.93 ± 0.56	14.27 ± 0.70	13.54 ± 0.65	0.759 ± 0.002	0.505 ± 0.005	0.530 ± 0.002	0.127 ± 0.008	0.194 ± 0.014	0.211 ± 0.015
79-118	16.03 ± 0.23	14.15 ± 0.33	13.27 ± 0.31	0.775 ± 0.003	0.594 ± 0.005	0.588 ± 0.002	0.157 ± 0.004	0.196 ± 0.007	0.217 ± 0.007
Average	20.94	14.91	14.18	0.752	0.554	0.557	0.096	0.180	0.196

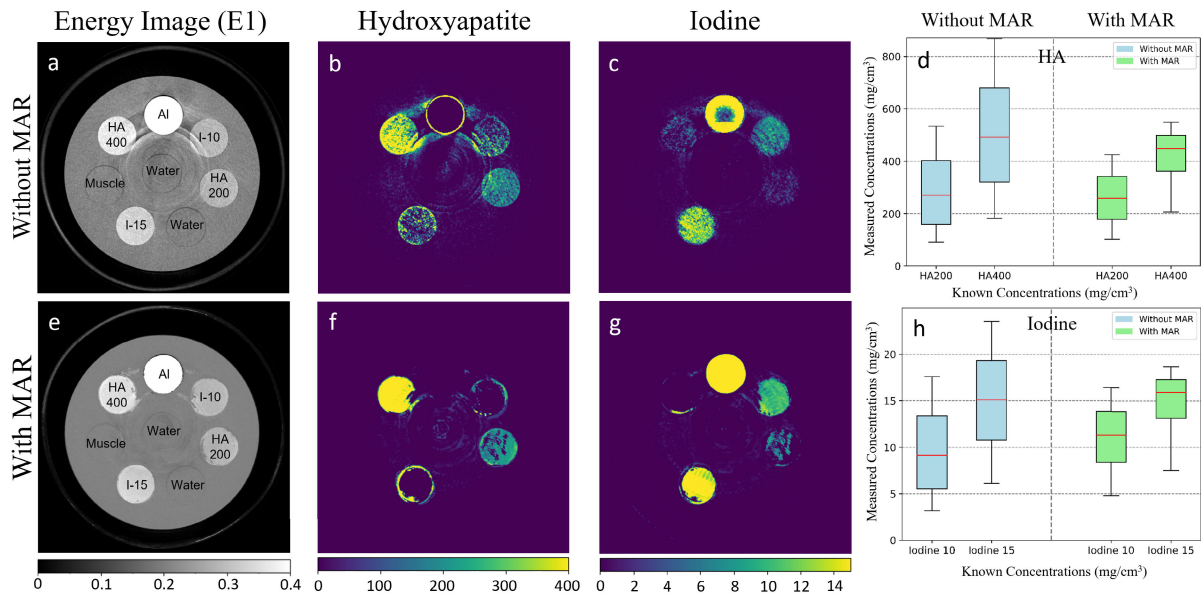


FIGURE 9. The results of the material analysis after using MAR algorithm. (a) shows the first energy bin image (7-40 keV) obtained from the SPCCT containing aluminium and material inserts. (b) and (c) show the material density images of hydroxyapatite (HA) and iodine obtained from the image shown in (a). (d) shows the box whiskers plot for HA with and without MAR. (e) shows the output obtained after MAR on (a). (f) and (g) show the material density images of HA and iodine-density images with MAR. (h) shows the box whiskers plot for iodine with and without MAR. The materials labels are 'Al' for aluminium, HA200 and 400 are for hydroxyapatite concentrations of 201.4 and 406.9 mg/cm³, respectively. I-10 and I-15 refers to iodine concentrations of 9.66, and 14.56 mg/cm³, respectively.

TABLE 4. Material Identification (sensitivity, specificity, accuracy, negative predictive value (NPV), and positive predictive value (PPV)) and Quantification (RMSE) analysis for material decomposition of hydroxyapatite (HA) and iodine(I) with and without metal artefact reduction (MAR), in the presence of aluminium insert. RMSE was estimated as a percent of known concentrations. "TP" stands for true positive values, "TN" stands for true negative values, "FP" stands for False positive values, and "FN" stands for false negative values.

Material (mg/cm ³)	Material Identification					Material Quantification
	Sensitivity (%) TP/(TP+FN)	Specificity (%) TN/(FP+TN)	Accuracy (%) (TN + TP)/ (TN+TP+FN+FP)	NPV (%) TN/(FN+TN)	PPV (%) TP/(TP+FP)	RMSE (mg/cm ³)
HA without MAR	74	90	86	91	73	0.937
HA with MAR	85	94	91	91	91	0.117
Iodine without MAR	72	89	84	88	74	0.049
Iodine with MAR	90	94	93	96	86	0.003

As illustrated in Fig. 5 (a), input images show significant streaking and overestimation in the attenuation coefficients across all energy bins. Moreover, an increase in the depth of ring artefacts was also observed, which is more prominent in the proximity of the metal inserts. Fig. 5 (c) shows the

corrected images resulted from the proposed MAR algorithm. The visual analysis of the two images shows a reduction in metal artefacts, ring artefacts, and noise levels.

In Fig. 6 (b) we can observe that aluminium has considerably less NLPV and cupping artefacts in the higher

energy bins as the peaks edges of the aluminium profile nearly vanish in these bins. Steel however, has much more prominent artefacts which did not insignificantly decrease at higher energies, as can be seen in Fig. 6 (f). Additionally, it was observed that the mean linear attenuation coefficient of the region containing steel increased with the increasing energy level, primarily due to the cupping artefact. The pronounced artefacts observed in steel arise mainly from its substantially higher density, 7.98 g/cm^3 , in contrast to the comparatively lower density of aluminium, 2.71 g/cm^3 . Nevertheless, the application of MAR algorithm effectively eliminates most of artefacts including NLPV, cupping artefacts, as well as noise for both metals, as shown in Fig. 6 (d,h).

Fig. 7 illustrates this observation, indicating that although the mean linear attenuation values of the output images closely match those of the simulated images, there is a consistent reduction in the spread or width of the histogram. This indicates that the algorithm corrects the images without affecting the attenuation profiles, thus maintaining the integrity of the extracted data. In Fig. 8 (b), the SNR of the output images is improved, indicating substantial noise reduction following the MAR algorithm's application. The lower RMSE (Fig. 8 (c)) suggests closer resemblance to artefact-free simulated images. Additionally, higher structural similarity (Fig. 8 (e)) compared to input images indicates improved preservation of spatial and attenuation profile integrity. This shows that the algorithm maintains the spatial and attenuation profile integrity while correcting the artefacts from the scan images.

Table. 3 shows that the RDU-Net outperforms the other two models across all metrics. However, the most significant change observed is in the RMSE values, where RDU-Net achieves significantly lower values. This indicates that the RDU-Net model not only achieves good structural similarity but also preserves the linear attenuation values, thereby retaining the spectral attenuation profiles of the scan effectively.

Furthermore, we conducted material analysis to assess the impact of MAR algorithm on MD. Fig. 9 (b) and (c) illustrate substantial loss of material information and miss-identification that occurs as a result of streaking and noise. However, after applying MAR algorithm, we observe an improvement in the density images of both HA and iodine, Fig. 9 (f) and (g), which shows more accurate material identification and decomposition. The box plot graphs for HA and iodine in Fig. 9 (d,h) similarly demonstrate these observations as the variations in the calculated densities for both materials decrease. This is evident from the reduction in the size of the box plots after implementing MAR algorithm. Moreover, the plot also reveals significant overlap between the box plots for both HA and iodine before MAR, leading to serious misquantification. Following the application of MAR, the quantification is improved and becomes more accurate with the median positioned closer to the actual values. Additionally, the box size is decreased in both plots, indicating enhanced accuracy in measurement. Furthermore, Table 4

provides statistical quantification of these enhancements, revealing improvements in all evaluation metrics following the implementation of MAR algorithm. The sensitivity and specificity for the detected concentrations of HA and iodine density images indicate their improved identification and quantification. The increased accuracy of both HA and iodine signifies a higher proportion of correct classifications. Even though the NPV remained the same for HA, it was increased for iodine, which indicates a better ability to correctly identify the absence of the materials. On the other hand, the PPV was increased significantly for both HA and iodine, suggesting a higher likelihood of correct identification when the materials are present. These improvements collectively highlight the enhanced performance of the algorithm in increasing the detection and quantification of materials by reducing noise and artefacts.

The present study has a few limitations. One of the primary challenges encountered early on was computational limitations. The photon counting CT data was substantial, with each slice measuring $5 \times 1300 \times 1300$ in dimensions. This necessitated a sophisticated and complex algorithm capable of detecting essential features. However, striking a balance between complexity and computational feasibility was crucial. Highly complex models strained our computing resources, affecting achievable accuracy. Managing model complexity and computational efficiency was challenging, sometimes requiring prioritization of efficiency over maximizing accuracy. Another prominent limitation is the reliance of the proposed framework on training datasets, restricting the model's performance to the specific data it has been trained on. Currently, the training data is derived solely from phantoms, providing information on a singular regular shape, thus rendering the model less effective when confronted with irregular shapes. The machine used in this study is a small-bore micro SPCCT, which lacks the capability to perform complex scans that simulate clinical settings. Additionally, due to its novelty, there is limited available data for SPCCT technology. To address this, future efforts are required to focus on the creation of a comprehensive biological training dataset that encompasses diverse metal shapes, placements, and types. This also necessitates the development of a sophisticated simulation framework for SPCCT capable of generating artefact-free images of complex geometries, a task beyond the capabilities of current simulation methods. Another limitation is that the current simulation process involves manual input for metal placements in artefact-free images, a difficult and time-consuming process. Due to this, the performance of the algorithm has not yet been validated on biological datasets, posing a challenge in its application to clinical settings. However, this is future work and we will conduct more studies in this regard for further optimization of our proposed framework.

V. CONCLUSION

The proposed RDU-Net has demonstrated promising results, exhibiting improvements in artefact-affected images across

all evaluation metrics. This advancement represents a significant step towards the development of a commercially viable MAR algorithm for multi-energy SPCCT. The algorithm not only effectively reduce artefacts but also retains comprehensive spectral information from the scans. This capability holds immense potential for facilitating advanced analyses, as evident from the results of MD presented in the paper.

REFERENCES

- [1] D. Esses, A. Birnbaum, P. Bijur, S. Shah, A. Gleyzer, and E. J. Gallagher, "Ability of CT to alter decision making in elderly patients with acute abdominal pain," *Amer. J. Emergency Med.*, vol. 22, no. 4, pp. 270–272, Jul. 2004.
- [2] F. A. Mettler Jr., B. R. Thomadsen, M. Bhargavan, D. B. Gilley, J. E. Gray, J. A. Lipoti, J. McCrohan, T. T. Yoshizumi, and M. Mahesh, "Medical radiation exposure in the U.S. in 2006: Preliminary results," *Health Phys.*, vol. 95, no. 5, pp. 502–507, 2008.
- [3] W. A. Kalender, "X-ray computed tomography," *Phys. Med. Biol.*, vol. 51, no. 13, p. R29, Jun. 2006, doi: [10.1088/0031-9155/51/13/R03](https://doi.org/10.1088/0031-9155/51/13/R03).
- [4] P. J. Withers, C. Bouman, S. Carmignato, V. Cnudde, D. Grimaldi, C. K. Hagen, E. Maire, M. Manley, A. Du Plessis, and S. R. Stock, "X-ray computed tomography," *Nature Rev. Methods Primers*, vol. 1, no. 1, p. 18, 2021.
- [5] S. Akashi-Tanaka, T. Fukutomi, N. Sato, and K. Miyakawa, "The role of computed tomography in the selection of breast cancer treatment," *Breast Cancer*, vol. 10, no. 3, pp. 198–203, Jul. 2003.
- [6] E. D. Nicol, B. L. Norgaard, P. Blanke, A. Ahmadi, J. Weir-McCall, P. M. Horvat, K. Han, J. J. Bax, and J. Leipsic, "The future of cardiovascular computed tomography: Advanced analytics and clinical insights," *Cardiovascular Imag.*, vol. 12, no. 6, pp. 1058–1072, 2019.
- [7] N. T. Wijesekera, M. K. Duncan, and S. P. Padley, "X-ray computed tomography of the heart," *Brit. Med. Bull.*, vol. 93, no. 1, pp. 49–67, 2010.
- [8] J. J. Battista, W. D. Rider, and J. Van Dyk, "Computed tomography for radiotherapy planning," *Int. J. Radiat. Oncol.*Biol.*Phys.*, vol. 6, no. 1, pp. 99–107, 1980.
- [9] P. G. Scribes and R. Yaparalvi, "Technical aspects of positron emission tomography/computed tomography in radiotherapy treatment planning," *Seminars Nucl. Med.*, vol. 42, no. 5, pp. 283–288, 2012.
- [10] L. Gjestebj, B. De Man, Y. Jin, H. Paganetti, J. Verburg, D. Giantsoudi, and G. Wang, "Metal artifact reduction in CT: Where are we after four decades?" *IEEE Access*, vol. 4, pp. 5826–5849, 2016.
- [11] H. Arabi and H. Zaidi, "Deep learning-based metal artefact reduction in PET/CT imaging," *Eur. Radiol.*, vol. 31, pp. 6384–6396, Feb. 2021.
- [12] H. Liao, W.-A. Lin, S. K. Zhou, and J. Luo, "ADN: Artifact disentanglement network for unsupervised metal artifact reduction," *IEEE Trans. Med. Imag.*, vol. 39, no. 3, pp. 634–643, Mar. 2020.
- [13] B. De Man, J. Nuyts, P. Dupont, G. Marchal, and P. Suetens, "Metal streak artifacts in X-ray computed tomography: A simulation study," in *Proc. IEEE Nucl. Sci. Symp. Conf. Rec. IEEE Nucl. Sci. Symp. Med. Imag. Conf.*, vol. 3, Nov. 1998, pp. 1860–1865.
- [14] F. E. Boas and D. Fleischmann, "CT artifacts: Causes and reduction techniques," *Imag. Med.*, vol. 4, no. 2, pp. 229–240, Apr. 2012.
- [15] A. Hunter and W. McDavid, "Characterization and correction of cupping effect artefacts in cone beam CT," *Dentomaxillofacial Radiol.*, vol. 41, no. 3, pp. 217–223, Mar. 2012.
- [16] J. Hsieh, *Computed Tomography: Principles, Design, Artifacts, and Recent Advances*. Bellingham, WA, USA: SPIE Press, 2003.
- [17] G. H. Glover and N. J. Pelc, "Nonlinear partial volume artifacts in X-ray computed tomography," *Med. Phys.*, vol. 7, no. 3, pp. 238–248, May 1980.
- [18] L. Sunwoo, S.-W. Park, J. H. Rhim, Y. Kang, Y. S. Chung, Y.-J. Son, and S. C. Kim, "Metal artifact reduction for orthopedic implants: Brain CT angiography in patients with intracranial metallic implants," *J. Korean Med. Sci.*, vol. 33, no. 21, p. e158, 2018.
- [19] A. Byl, L. Klein, S. Sawall, S. Heinze, H. Schlemmer, and M. Kachelrieß, "Photon-counting normalized metal artifact reduction (NMAR) in diagnostic CT," *Med. Phys.*, vol. 48, no. 7, pp. 3572–3582, Jul. 2021.
- [20] H. Yu, K. Zeng, D. K. Bharkhada, G. Wang, M. T. Madsen, O. Saba, B. Policeni, M. A. Howard, and W. R. K. Smoker, "A segmentation-based method for metal artifact reduction," *Academic Radiol.*, vol. 14, no. 4, pp. 495–504, Apr. 2007.
- [21] P. Midthun, E. Kirkhus, B. H. Østerås, P. R. Høines, A. England, and S. Johansen, "Metal artifact reduction on musculoskeletal CT: A phantom and clinical study," *Eur. Radiol. Exp.*, vol. 7, no. 1, p. 46, Jul. 2023.
- [22] M. Zhu, Q. Zhu, Y. Song, Y. Guo, D. Zeng, Z. Bian, Y. Wang, and J. Ma, "Physics-informed sinogram completion for metal artifact reduction in CT imaging," *Phys. Med. Biol.*, vol. 68, no. 6, Mar. 2023, Art. no. 065006.
- [23] A. J. Vellarackal and A. H. Kaim, "Metal artefact reduction of different alloys with dual energy computed tomography (DECT)," *Sci. Rep.*, vol. 11, no. 1, p. 2211, Jan. 2021.
- [24] D. Richtsmeier, P.-A. Rodesch, K. Iniewski, W. Siu, and M. Bazalova-Carter, "The feasibility of accurate stent visualization with photon-counting detector CT and K-edge imaging," *IEEE Trans. Radiat. Plasma Med. Sci.*, vol. 7, no. 7, pp. 712–718, Sep. 2023.
- [25] S. Skornitzke, V. Mergen, J. Biederer, H. Alkadhi, T. D. Do, W. Stiller, T. Frauenfelder, H.-U. Kauczor, and A. Euler, "Metal artifact reduction in photon-counting detector CT: Quantitative evaluation of artifact reduction techniques," *Investigative Radiol.*, vol. 59, no. 6, pp. 442–449, 2023.
- [26] S. Puvanasantharajah, D. Fontanarosa, M. Wille, and S. M. Camps, "The application of metal artifact reduction methods on computed tomography scans for radiotherapy applications: A literature review," *J. Appl. Clin. Med. Phys.*, vol. 22, no. 6, pp. 198–223, Jun. 2021.
- [27] A.-S. Björkman, A. Malusek, H. Gauffin, A. Persson, and S. K. Koskinen, "Spectral photon-counting CT: Image quality evaluation using a metal-containing bovine bone specimen," *Eur. J. Radiol.*, vol. 168, Nov. 2023, Art. no. 111110.
- [28] M. Danielsson, M. Persson, and M. Sjölin, "Photon-counting X-ray detectors for CT," *Phys. Med. Biol.*, vol. 66, no. 3, Feb. 2021, Art. no. 03TR01.
- [29] T. Flohr, S. Ulzheimer, M. Petersilka, and B. Schmidt, "Basic principles and clinical potential of photon-counting detector CT," *Chin. J. Academic Radiol.*, vol. 3, no. 1, pp. 19–34, Mar. 2020.
- [30] A. Raja, M. Moghiseh, C. Bateman, N. De Ruiter, B. Schon, N. Schleich, T. Woodfield, A. Butler, and N. Anderson, "Measuring identification and quantification errors in spectral CT material decomposition," *Appl. Sci.*, vol. 8, no. 3, p. 467, Mar. 2018.
- [31] E. Marfo, N. G. Anderson, A. P. H. Butler, N. Schleich, P. Carbonez, J. Damet, C. Lowe, J. Healy, A. I. Chernoglazov, M. Moghiseh, M. Collaboration, and A. Y. Raja, "Assessment of material identification errors, image quality, and radiation doses using small animal spectral photon-counting CT," *IEEE Trans. Radiat. Plasma Med. Sci.*, vol. 5, no. 4, pp. 578–587, Jul. 2021.
- [32] R. Aamir et al., "MARS spectral molecular imaging of Lamb tissue: Data collection and image analysis," *J. Instrum.*, vol. 9, no. 2, Feb. 2014, Art. no. P02005, doi: [10.1088/1748-0221/9/02/P02005](https://doi.org/10.1088/1748-0221/9/02/P02005).
- [33] M. Simard, R. K. Panta, S. T. Bell, A. P. Butler, and H. Bouchard, "Quantitative imaging performance of MARS spectral photon-counting CT for radiotherapy," *Med. Phys.*, vol. 47, no. 8, pp. 3423–3434, 2020.
- [34] L. K. Stamp, N. G. Anderson, F. Becce, M. Rajeswari, M. Polson, O. Guyen, A. Viry, C. Choi, T. E. Kirkbride, and A. Y. Raja, "Clinical utility of multi-energy spectral photon-counting computed tomography in crystal arthritis," *Arthritis Rheumatol.*, vol. 71, no. 7, pp. 1158–1162, Jul. 2019.
- [35] B. Zhou, X. Chen, S. K. Zhou, J. S. Duncan, and C. Liu, "DuDoDR-net: Dual-domain data consistent recurrent network for simultaneous sparse view and metal artifact reduction in computed tomography," *Med. Image Anal.*, vol. 75, Jan. 2022, Art. no. 102289.
- [36] T. Lyu, Z. Wu, G. Ma, C. Jiang, X. Zhong, Y. Xi, Y. Chen, and W. Zhu, "PDS-MAR: A fine-grained projection-domain segmentation-based metal artifact reduction method for intraoperative CBCT images with guidewires," 2023, *arXiv:2306.11958*.
- [37] L. Gjestebj, Q. Yang, Y. Xi, H. Shan, B. Claus, Y. Jin, B. De Man, and G. Wang, "Deep learning methods for CT image-domain metal artifact reduction," in *Developments in X-Ray Tomography XI*, vol. 10391. Bellingham, WA, USA: SPIE, 2017, pp. 147–152.
- [38] E. Meyer, R. Raupach, M. Lell, B. Schmidt, and M. Kachelrieß, "Normalized metal artifact reduction (NMAR) in computed tomography," *Med. Phys.*, vol. 37, no. 10, pp. 5482–5493, Oct. 2010.
- [39] L. Zhu, Y. Han, L. Li, X. Xi, M. Zhu, and B. Yan, "Metal artifact reduction for X-ray computed tomography using U-Net in image domain," *IEEE Access*, vol. 7, pp. 98743–98754, 2019.
- [40] L. Yu, Z. Zhang, X. Li, H. Ren, W. Zhao, and L. Xing, "Metal artifact reduction in 2D CT images with self-supervised cross-domain learning," *Phys. Med. Biol.*, vol. 66, no. 17, Sep. 2021, Art. no. 175003.

- [41] Y. Zhang and H. Yu, "Convolutional neural network based metal artifact reduction in X-ray computed tomography," *IEEE Trans. Med. Imag.*, vol. 37, no. 6, pp. 1370–1381, Jun. 2018.
- [42] W.-A. Lin, H. Liao, C. Peng, X. Sun, J. Zhang, J. Luo, R. Chellappa, and S. K. Zhou, "DuDoNet: Dual domain network for CT metal artifact reduction," in *Proc. IEEE/CVF Conf. Comput. Vis. Pattern Recognit. (CVPR)*, Jun. 2019, pp. 10512–10521.
- [43] M. A. A. Hegazy, M. H. Cho, M. H. Cho, and S. Y. Lee, "U-net based metal segmentation on projection domain for metal artifact reduction in dental CT," *Biomed. Eng. Lett.*, vol. 9, no. 3, pp. 375–385, Aug. 2019.
- [44] Z. Lai, L. Li, and W. Cao, "Metal artifact reduction with deep learning based spectral CT," in *Proc. 14th Int. Congr. Image Signal Process., Biomed. Eng. Informat. (CISP-BMEI)*, Oct. 2021, pp. 1–4.
- [45] M. Busi, C. Kehl, J. R. Frisvad, and U. L. Olsen, "Metal artifact reduction in spectral X-ray CT using spectral deep learning," *J. Imag.*, vol. 8, no. 3, p. 77, Mar. 2022.
- [46] R. Ballabriga, J. Aloyz, G. Blaj, M. Campbell, M. Fiederle, E. Frojdh, E. Heijne, X. Llopert, M. Pichot, S. Procz, L. Tlustos, and W. Wong, "The Medipix3RX: A high resolution, zero dead-time pixel detector readout chip allowing spectroscopic imaging," *J. Instrum.*, vol. 8, no. 2, 2013, Art. no. C02016.
- [47] R. Aamir, S. Lansley, R. Zainon, M. Fiederle, A. Fauler, D. Greiffenberg, P. Butler, and A. Butler, "Pixel sensitivity variations in a CdTe-Medipix2 detector using poly-energetic X-rays," *J. Instrum.*, vol. 6, no. 1, 2011, Art. no. C01059.
- [48] K. He, X. Zhang, S. Ren, and J. Sun, "Deep residual learning for image recognition," in *Proc. IEEE Conf. Comput. Vis. Pattern Recognit. (CVPR)*, Jun. 2016, pp. 770–778.
- [49] G. Huang, Z. Liu, L. Van Der Maaten, and K. Q. Weinberger, "Densely connected convolutional networks," in *Proc. IEEE Conf. Comput. Vis. Pattern Recognit. (CVPR)*, Jul. 2017, pp. 4700–4708.
- [50] O. Ronneberger, P. Fischer, and T. Brox, "U-net: Convolutional networks for biomedical image segmentation," in *Proc. 18th Int. Conf. Med. Image Comput. Comput.-Assist. Intervent. (MICCAI)*, Munich, Germany: Springer, 2015, pp. 234–241.
- [51] H. Zhao, O. Gallo, I. Frosio, and J. Kautz, "Loss functions for neural networks for image processing," 2015, *arXiv:1511.08861*.
- [52] K. Simonyan and A. Zisserman, "Very deep convolutional networks for large-scale image recognition," 2014, *arXiv:1409.1556*.
- [53] Y. Zhu, X. Liang, L. Deng, C. Zhang, X. Zhou, Y. Xie, and H. Zhang, "CT metal artifact correction assisted by the deep learning-based metal segmentation on the projection domain," in *Proc. IEEE Int. Conf. Med. Imag. Phys. Eng. (ICMIPE)*, Nov. 2021, pp. 1–10.
- [54] P. Gayathri, A. Dhavileswarapu, S. Ibrahim, R. Paul, and R. Gupta, "Exploring the potential of VGG-16 architecture for accurate brain tumor detection using deep learning," *J. Comput., Mech. Manage.*, vol. 2, no. 2, pp. 13–22, Jun. 2023.
- [55] Z.-P. Jiang, Y.-Y. Liu, Z.-E. Shao, and K.-W. Huang, "An improved VGG16 model for pneumonia image classification," *Appl. Sci.*, vol. 11, no. 23, p. 11185, Nov. 2021.
- [56] C. J. Bateman et al., "MARS-MD: Rejection based image domain material decomposition," *J. Instrum.*, vol. 13, May 2018, Art. no. P05020.



OSAMA KHAN received the bachelor's degree in applied physics from NED University, Karachi, Pakistan, in 2019. He is currently pursuing the master's degree in biomedical sciences (BMES) with the School of Mechanical and Manufacturing Engineering (SMME), National University of Science & Technology (NUST), Islamabad, Pakistan. He is also a Research Assistant with the Physics Department, Khalifa University, United Arab Emirates. His research interests include

medical physics, biomedical engineering, machine/deep learning, and computer vision, with a current focus on scientific investigations in medical image analysis. He is pioneering advancements in material decomposition

and metal artefacts removal using machine/deep learning techniques. His work aims to revolutionize medical imaging by utilizing spectral imaging capabilities to minimize metal artefacts, while integrating machine learning to develop advanced artefact reduction algorithms. Through his research, he is establishing new standards for precision and effectiveness in medical diagnostic tools, thereby advancing the field of medical imaging.



BRIYA TARIQ received the B.S. degree in electronics from Government College University, Pakistan, in 2014, and the M.S. degree in microelectronics engineering and semiconductor physics from the University of Punjab, Pakistan, in 2016. She is currently pursuing the Ph.D. degree in physics with the Khalifa University of Science and Technology, United Arab Emirates.

Her Ph.D. research is revolutionizing medical imaging by enhancing spectral imaging techniques to reduce metal artefacts and integrating machine learning to develop sophisticated artefact reduction algorithms. Multi-energy CT technology, her work is setting new benchmarks in the precision and effectiveness of medical diagnostic tools, thereby elevating the field of medical imaging. From 2016 to 2017, she was a Research Assistant with the Department of Solid State Physics, University of Punjab, Pakistan. She worked on the simulation of a polymeric-based piezoelectric actuator during her bachelor's research work and she worked on an exploration of the advanced materials for nanotube formation during the master's research project. Her research interests include developing novel materials and devices for electronics and healthcare, enhancing imaging technologies for medical diagnostics, and exploring the intersection of physics and technology to address complex scientific and engineering challenges.



NADINE FRANCIS received the B.Sc. degree in systems and biomedical engineering from Cairo University, Egypt, in 2013, the joint M.Sc. degree in bioengineering and innovation and in neuroscience from Paris Descartes University and École Supérieure de Physique et de Chimie Industrielles (ESPCI-ParisTech), France, in 2015, and the Ph.D. degree in bioengineering from the Imperial College London, in 2022. Currently, she holds the position of a Postdoctoral Fellow with

the Medical Physics Department, Khalifa University. Prior to this role, she made significant contributions to the neuroscience field, concentrating on the advancement of brain machine interfaces and tools for evaluating navigation abilities in various diseases. Moreover, she was a Senior Research Scientist and a Postdoctoral Fellow with the Biomedical Engineering and Innovation Laboratory for Cardiovascular Diseases. With her extensive expertise in biomedical engineering, artificial intelligence, machine learning, and signal and image processing, she brings over nine years of experience in developing innovative solutions and deploying advanced machine learning models for image recognition and analysis, with the aim of pioneering revolutionary advancements in healthcare.



NABIL MAALEJ received the B.S. degree in EE from the University of Rochester, NY, USA, in 1985, and the M.S. degree in electrical engineering and the M.S. and Ph.D. degrees in medical physics from the University of Wisconsin-Madison, in 1987, 1990, and 1994, respectively. He joined Khalifa University, in 2021, as an Associate Professor in medical physics. Before, he was a Faculty Member of the Physics Department, King Fahd University of Petroleum, from 2001 to 2021. Previously, he was a Consultant in the design and development of medical devices at Arthur D. Little Inc., Boston, from 1998 to 2001. Before that, he was a Research Associate with the Cardiovascular Research Laboratory, University of Wisconsin-Madison, from 1994 to 1998, and as a Research Assistant, from 1990 to 1994. His research interests include medical physics and biomedical instrumentation in general and in particular the optimization of medical imaging, the development of nanoparticles for X-ray and MRI imaging, the development of new parametric imaging techniques, and the application of AI to medical imaging and radiation therapy. In the last five years, he worked on AI applications in medical physics including radiation therapy and cancer imaging. Since 2021, he has been working on research related to spectral CT imaging, including phantom design, contrast material design and imaging, material decomposition, and parametric imaging. His experience in spectral CT imaging and material decomposition is very relevant to the proposed research. He is a member of American Association of Physicists in Imaging (AAPM).



ASIM WARIS (Member, IEEE) received the B.Sc. degree in mechatronics engineering and the master's degree in biomedical engineering from the National University of Sciences & Technology (NUST), Pakistan, in 2011 and 2013, respectively, and the Ph.D. degree from the Department of Health Science and Technology, Aalborg University, in 2018. He is currently an Assistant Professor with NUST. His research interests include EMG signal processing, pattern recognition, deep learning, and myoelectric prosthetic control.



ABDERAOUF BEHOUCHE received the bachelor's degree in applied physics (medical) and the master's degree in medical physics from Ferhat Abbas Setif 1 University, Algeria, in 2018 and 2020, respectively, where he is currently pursuing the Ph.D. degree in medical physics. Additionally, he is also a Research Associate with the College of Engineering, Khalifa University, Abu Dhabi, United Arab Emirates. His research interests include medical image processing, image registration and segmentation, and X-ray systems.



AMER KASHIF received the Ph.D. degree from the University of Canterbury, New Zealand. He is currently a Distinguished Academician and a Researcher specializing in bioengineering and electrical engineering. He is also a TSO. His research interest includes imaging technology for breast cancer screening systems. He has received numerous awards, including the Tamgha-i-Imtiaz (Military) and has authored over 30 peer-reviewed journal articles and more than 22 peer-reviewed conference proceedings. With extensive experience in academia and industry, he has held various leadership positions, including as an Associate Professor with the National University of Sciences & Technology (NUST), Islamabad. He has also contributed significantly to the development of medical equipment policies and initiatives, including the Advisor on Medical Equipment for the USAID Global Health Supply Chain Program. He is also the Additional Registrar with Pakistan Engineering Council's Innovation & Entrepreneurship Development Centre, where he plays a pivotal role in fostering innovation and entrepreneurship in Pakistan's engineering sector.



AAMIR RAJA is currently an Assistant Professor with Khalifa University, United Arab Emirates, and an Honorary Senior Research Fellow with the University of Otago Christchurch, New Zealand. He is also the Co-Founder of the Medical Physics Wing with the Physics Department and played a key role in developing an accredited M.Sc. Program in Medical Physics. His research endeavors have received support from various New Zealand and United Arab Emirates funding agencies, the University of Otago, New Zealand, Khalifa University, private foundations, and industry. His previous roles include serving as a Senior Research Fellow of the Department of Academic Radiology, University of Otago, Christchurch, New Zealand, and as a Visiting Academic Teaching Staff with the ARA Institute of Canterbury, New Zealand. He also held a secondment position in the industry and significantly contributed to the development of the world's first commercial spectral photon-counting computed tomography for cutting-edge multidisciplinary biomedical research, enabling the production of color x-ray images with applications in biology and medicine. His academic achievements in the field of spectral CT imaging have been widely recognized by his peers and the medical imaging community. He has authored over 68 publications, with a majority of them as the senior, first, or second author. These include over more than 30 peer-reviewed journal articles, more than 22 peer-reviewed conference proceedings, more than 45 published abstracts, and two book chapters.

Dr. Raja is a Life Member and a fellow of the Union for International Cancer Control. He served as a Guest Editor for a Special Issue of IEEE Access Dedicated to Multidisciplinary Biomedical Imaging Research.

...